AIMS Mathematics, 11(6): 17293–17319.
DOI: 10.3934/math.2026708
Received: 08 April 2026
Revised: 21 May 2026
Accepted: 27 May 2026
Published: 15 June 2026

https://www.aimspress.com/journal/Math

Research article

Benchmark travelling waves and bidirectional adaptive DA–PMA computation for the two-dimensional regularized long-wave equation

H. S. Alayachi and A. R. Alharbi*

Department of Mathematics, College of Science, Taibah University, Medina 42353, Saudi Arabia

* **Correspondence:** Email: arharbi@taibahu.edu.sa.

Abstract: This paper presents an adaptive computational framework for the two-dimensional regularized long-wave (RLW) equation. The main focus was on the numerical treatment of the model on moving nonuniform meshes. The RLW equation was first rewritten in a mixed differential-algebraic (DA) form by introducing an auxiliary variable. This reformulation avoids the direct discretization of the mixed space–time derivatives and leads to a more convenient adaptive implementation. The spatial approximation was constructed on bidirectionally adaptive tensor-product grids using five-point Fornberg finite-difference operators. Mesh redistribution was performed through a parabolic Monge–Ampère (PMA) rezoning strategy combined with monitor functions and shape-preserving interpolation between successive meshes. Exact travelling-wave solutions were also derived through an oblique wave reduction. These solutions were used mainly as benchmark data for the numerical computations. In particular, the solitary-wave solution provides compatible initial conditions, boundary data, auxiliary-field values, and reference profiles for error measurement. The stability discussion was carried out under admissible mesh evolution. On each frozen mesh, the spatial approximation was formally second-order consistent. The convergence behavior of the full adaptive algorithm was assessed numerically because mesh redistribution and inter-mesh interpolation introduce additional error effects. Numerical experiments were presented for single-wave and two-pulse configurations. The results show that the adaptive method preserves the wave structure with good accuracy and produces smaller errors than the corresponding fixed-mesh computation. The adaptive meshes remained concentrated near the dominant wave regions while maintaining global mesh regularity throughout the simulation.

Keywords: two-dimensional regularized long-wave equation; adaptive moving meshes; mixed differential-algebraic formulation; parabolic Monge–Ampère redistribution; bidirectional adaptive computation; travelling-wave benchmark solutions; nonuniform finite differences
Mathematics Subject Classification: 35C07, 35Q35, 35Q53, 65M06, 65M12, 65M50

1. Introduction

The regularized long-wave (RLW) equation, also known as the Benjamin–Bona–Mahony equation, is a fundamental nonlinear dispersive model for the propagation of long waves in fluids and other continuous media. In two spatial dimensions, a commonly used form of the equation is

$$u_t + \alpha u_x + \beta u_y + \gamma u\, u_x + \delta u\, u_y - \mu u_{xxt} - \mu u_{yyt} = 0, \qquad (x, y) \in \Omega, \quad t \in (0, T], \tag{1.1}$$

supplemented with suitable initial and boundary conditions, where $u = u(x, y, t)$ denotes the wave profile, $\Omega \subset \mathbb{R}^2$ is a bounded spatial domain, and the coefficients $\alpha, \beta, \gamma, \delta$, and μ are real constants satisfying $\mu > 0$ and $|\gamma| + |\delta| > 0$.

The historical development of the RLW equation is closely connected with the mathematical theory of weakly nonlinear dispersive waves. Its origins are commonly traced to Peregrine's analysis of undular bore development, after which Benjamin, Bona, and Mahony established the model as an alternative to the classical Korteweg–de Vries (KdV) equation for the description of small-amplitude long waves propagating in channels [1, 2].

The RLW equation's purpose is not to introduce another long-wave model but to strive for a balance between weak nonlinearity and dispersion, in a way that is regularized and physically meaningful. The one-dimensional formulation came first. The two-dimensional version arises naturally when considering wave motion that is not purely unidirectional and, in that case, must include transverse effects [3, 4]. Although the RLW equation is qualitatively similar to the KdV equation, analytically, it is quite different. For example, the KdV equation is completely integrable and has an infinite number of conservation laws, while the RLW equation has a very small number of conservation laws, and only a few of those laws are independent [5]. However, the RLW equation is believed to be a reasonable and physically realistic alternative to the KdV equation for many applications because of the essential dispersive characteristics of the nonlinear oscillatory motion that it describes [6]. Moreover, while the RLW equation does not possess an inverse-scattering formalism like the KdV equation, the solutions of the RLW equation exhibit the same characteristic dispersive behavior, including solitary waves with oscillatory tails [7].

The mathematical simplicity of the RLW equation, together with its physical relevance, has attracted considerable attention over the years. Bona et al. [8] investigated stable and unstable solitary-wave solutions of the generalized RLW equation. Tian et al. [9] studied a two-dimensional RLW model motivated by problems in fluid dynamics and plasma physics. Related analytical and transformation-based methods for nonlinear evolution equations were also developed by Ma and Fuchssteiner [10] and by Matveev and Salle [11].

In the steadily evolving RLW-type models, the latest research in *AIMS Mathematics* has noted the benefit of integrating exact travelling-wave constructions with dependable computational verification for nonlinear dispersive systems. In particular, *AIMS Mathematics* has presented some of the first examples of analytical-numerical studies in the context of the Novikov-Veselov system, generalized breaking soliton equations, and some related multidimensional wave models, where the wave formations were first computed and then validated using either stable finite-difference or adaptive mesh frameworks [12–14]. These studies affirm that the synergy of symbolic travelling-wave analysis with structurally aware computation is an applicable strategy for nonlinear wave issues in greater dimensions.

The individual elements of (1.1) help us understand the equation's significance in modelling. The term u_t represents the temporal local evolution of the wave field. The linear transport terms, αu_x and βu_y, describe propagation in the main spatial variables; these terms characterize the basic advection of the disturbance through the medium. The nonlinear terms, $\gamma u, u_x$, δu and u_y, account for amplitude-dependent steepening, indicating that the local speed of propagation is wave amplitude dependent. The regularizing terms $-\mu u_{xxt}$ and $-\mu u_{yyt}$, on the other hand, introduce dispersive effects in both directions and offset excessive nonlinear steepening. μ quantifies the strength of the dispersive regularization. The parameters α and β determine the scales of linear propagation, while γ and δ capture the strength of nonlinear transport. Thus, the RLW equation can be considered as a delicate balance of transport, nonlinearity, and dispersion. The two-dimensional RLW equation's application to various physically relevant cases is due to its structural balance. First, in shallow-water hydrodynamics, it acts as a model for small-amplitude long surface waves and nonlinear transverse wave propagation in channel-like configurations where both weak nonlinearity and finite dispersion need to be considered [1, 2]. Here, this equation is closely related to the analysis of undular bores and long-wave propagating over extended spatial intervals. Second, in plasma physics, RLW-type models describe waves of ion-acoustics and waves of magneto-hydrodynamics, where the interplay of nonlinear steepening and dispersive spreading governs the mechanisms of formation and interaction of localized travelling structures [8]. Third, the equation is applicable in the case of solid and multi-phase media, where it models longitudinal dispersive waves in elastic rods and waves of pressure in liquid gas mixtures or bubbly media [2, 8]. In all of these applications, RLW models provide an attractive intermediate description, which is significantly less complicated than the complete physical models, but still sufficiently complicated to capture interesting and scientifically relevant wave phenomena. In terms of computation, the latest research has also revealed that adaptive mesh redistribution is of particular value for nonlinear oscillatory equations which possess a localized, dynamically steepening, or widely interacting solution. In this regard, mesh-moving-based adaptive strategies and Monge–Ampère (PMA)-type redistribution have been applied in a positive way to nonlinear time-dependent equations in one-dimensional and two-dimensional, where active wave regions receive better resolution, and greater efficiency is attained than from corresponding fixed-mesh discretizations [15, 16]. These data provide a solid basis for applying adaptive spatial redistribution within dispersive oscillatory models where significant structures exist in a relatively small region of a large computational domain. The form of (1.1) is considered because it extends the classical one-dimensional RLW equation to two spatial directions. The one-dimensional model is appropriate when the wave motion is mainly longitudinal. The two-dimensional model allows the wave field to vary in both spatial variables. This makes it more suitable for oblique waves, transverse variations, and spatially localized structures. The additional terms in the y-direction improve the description of physical wave patterns that cannot be represented accurately by a single spatial coordinate. Table 1 gives a short comparison between the one-dimensional and two-dimensional RLW models.

Table 1. Comparison between the one-dimensional RLW model and the two-dimensional RLW model used in this study.

Aspect	One-dimensional RLW model	Two-dimensional RLW model (1.1)
Spatial dependence	The wave depends on a single spatial variable, usually x.	The wave depends on both spatial variables, x and y.
Propagation behavior	Mainly describes longitudinal wave propagation.	Allows oblique propagation and transverse wave variation.
Physical setting	Suitable for narrow or effectively one-dimensional media.	More appropriate for wider domains with transverse wave effects.
Dispersive regularization	Includes longitudinal regularization through terms such as u_{xxt}.	Includes regularization in both spatial directions through u_{xxt} and u_{yyt}.
Numerical difficulty	Requires resolution mainly in one spatial direction.	Requires adaptive resolution in both spatial directions.
Role in this work	Used mainly for comparison and numerical reference.	Serves as the main model for the adaptive mixed differential-algebraic (DA)–PMA method.

The present study is motivated by these considerations and by the need for a numerically robust framework that remains faithful to the underlying dispersive structure of the model. Our first objective is to construct a generalized adaptive numerical framework for the RLW equation based on a mixed differential-algebraic formulation and a bidirectional PMA/rezoning strategy on nonuniform tensor-product grids. In realistic simulations, large computational domains are often required in order to suppress artificial boundary effects and to capture localized dispersive structures over long time intervals. Under such circumstances, a uniform mesh may become prohibitively expensive, particularly in two dimensions. Adaptive mesh redistribution is therefore especially attractive, since it allows the computational grid to track the evolving geometry of the solution and to place numerical resolution only where it is genuinely needed.

In this research, the aforementioned adaptive approach is achieved through directional monitoring-based rezoning in both considered spatial dimensions, in conjunction with non-uniform finite-difference operators and mesh transfers that preserve the shape of the solution across successive meshes. This approach ensures an effective compromise between adaptable geometry, computational efficiency, and local accuracy in the proximity of the dominant wave regions. Alongside the numerical goals, this study includes an analytical aspect aiming for the construction of exact travelling-wave benchmarks for the two-dimensional RLW equation. More specifically, we reduce the governing partial differential equation to a nonlinear ordinary differential equation via an oblique travelling-wave transformation, and then apply two exact-solution methods, the Riccati equation method, and a generalized Arnous-type method [17]. With these methods, we obtain regular solitary-wave forms and additional closed-form solutions that allow for singular and periodic solutions, which are then used in the numerical section. Specifically, the analytical solution that we obtain is a smooth localized solitary wave that will serve as the reference solution to construct compatible initial and boundary conditions, as well as evaluate the accuracy of the adaptive computations.

Our second objective is to address the mixed space-time derivatives in (1.1). This issue is particularly important when the equation is discretized on a moving non-uniform grid. RLW-type

equations belong to a broader class of evolutionary partial differential equations with mixed derivatives, including the Boussinesq, modified Buckley–Leverett, and Sobolev equations [18–20]. To handle this difficulty, we introduce an auxiliary variable and rewrite the RLW equation as a coupled mixed system. This reformulation avoids the direct treatment of the mixed space-time derivatives and gives a suitable framework for adaptive semi-discretization on moving non-uniform grids.

The two-dimensional RLW equation remains a staple in contemporary numerical analysis due to its rich historical context, physical relevance, mathematical finesse, and interesting computational aspects. Its study therefore provides a natural and demanding setting for the design of adaptive, robust, and structure-aware numerical methods capable of resolving localized dispersive wave phenomena with high fidelity. The novelty of the present work is mainly numerical rather than purely analytical. The travelling-wave solutions are used primarily as benchmark data for the adaptive numerical computations. They provide exact initial conditions, boundary values, auxiliary-field data, and reference profiles for error evaluation. The main contribution of the paper is the mixed differential-algebraic reformulation of the two-dimensional RLW equation. The proposed method is implemented on bidirectionally adaptive nonuniform tensor-product meshes. The framework further combines PMA-based mesh redistribution, five-point Fornberg finite-difference discretization, and shape-preserving inter-mesh transfer within a unified adaptive moving-mesh setting.

The remainder of this paper is organized as follows. Section 2 is devoted to the construction of exact travelling-wave solutions and their associated benchmark fields. Section 3 presents the mixed reformulation, the PMA-based semi-discretization, and the stability and convergence properties of the adaptive RLW solver. Section 4 contains the numerical experiments for the generalied adaptive framework in one and two spatial dimensions. Finally, Section 5 summarizes the main conclusions and outlines possible directions for future research.

2. Exact travelling-wave solutions via two efficient analytical approaches

This section derives travelling-wave benchmark solutions for the two-dimensional RLW equation. The aim is not to present the exact-solution construction as the main novelty of the paper, but rather to obtain mathematically compatible benchmark profiles for the adaptive numerical framework developed later. These solutions provide exact initial conditions, boundary data, auxiliary-field values, and reference profiles for the quantitative assessment of the proposed adaptive method. The Riccati equation framework is employed here as a constructive analytical tool for deriving benchmark travelling-wave solutions suitable for validating the proposed adaptive numerical framework. In particular, using the Riccati equation approach and by the generalized Arnous-type representation, we construct explicit wave profiles for the present two-dimensional RLW model in a form suitable for subsequent numerical verification. The travelling-wave construction below is based directly on the governing two-dimensional RLW equation introduced in Eq (1.1).

To seek obliquely propagating travelling waves, we introduce the reduction

$$u(x, y, t) = U(\xi), \qquad \xi = kx + \ell y - ct - \xi_0, \tag{2.1}$$

where k and ℓ denote the wave numbers in the x- and y-directions, respectively, c is the constant wave speed in the travelling coordinate, and ξ_0 is an arbitrary phase shift.

Substituting (2.1) into (1.1) and integrating once under the standard localized far-field conditions yields the reduced nonlinear ordinary differential equation

$$\mu c(k^2 + \ell^2)U'' + (\alpha k + \beta \ell - c)U + \frac{\gamma k + \delta \ell}{2} U^2 = 0. \tag{2.2}$$

This reduction is consistent with the standard travelling-wave framework used for related nonlinear dispersive wave equations [17]. The resulting solitary-wave profile is introduced here as an exact benchmark for the adaptive mixed formulation developed in the subsequent numerical section. For notational convenience, we write

$$a = \mu c(k^2 + \ell^2), \qquad b = \alpha k + \beta \ell - c, \qquad d = \frac{\gamma k + \delta \ell}{2}, \tag{2.3}$$

so that (2.2) becomes

$$aU'' + bU + dU^2 = 0. \tag{2.4}$$

2.1. Outline of the analytical construction methods

This subsection gives a short outline of the two analytical methods used below. Both methods are applied to the reduced travelling-wave Eq (2.4). Their role here is to produce explicit benchmark profiles for the adaptive numerical tests. The first method is the Riccati-equation expansion method. The solution is assumed to be a finite polynomial in an auxiliary function $R(\xi)$. The degree of this polynomial is chosen by the balance rule. In (2.4), the highest derivative term U'' is balanced with the nonlinear term U^2. This gives a quadratic form in $R(\xi)$. The auxiliary function $R(\xi)$ is then taken to satisfy a Riccati equation. Different choices of the Riccati parameters give hyperbolic, singular hyperbolic, and trigonometric branches. The second method is the generalized Arnous-type representation. It uses the ratio $\Phi'(\xi)/\Phi(\xi)$ as the auxiliary quantity. The same balance rule again gives a quadratic form. The auxiliary relation for Φ then leads to similar hyperbolic and trigonometric branches. These include the sech^2, csch^2, $\sec^2$, and $\csc^2$ solutions reported below. These methods are used here as constructive tools, not as the main novelty of the paper. The main purpose is to obtain smooth travelling-wave data for the mixed adaptive DA–PMA computation. The general construction follows the approach described in [17].

2.2. Riccati-equation construction

Among the two possible analysis approaches, the Riccati equation approach is the most natural for the RLW reduction since Eq (2.4) is a second-order nonlinear wave equation with quadratic nonlinearity.

The polynomial representation in (2.5) follows the standard balance principle used in Riccati-type expansion methods. For the reduced Eq (2.2), the highest derivative term U'' and the nonlinear term U^2 determine the degree of the ansatz. Balancing these two contributions gives a quadratic expansion in the auxiliary Riccati function $R(\xi)$. Therefore, the finite expansion is taken up to $R^2(\xi)$. The Riccati equation in Eq (2.7) is then used to convert the reduced nonlinear differential equation into an algebraic system for the unknown coefficients. This approach is a standard symbolic construction technique for nonlinear travelling-wave reductions [17].

In accordance with this approach, we seek the solution in the polynomial form

$$U(\xi) = A_0 + A_1 R(\xi) + A_2 R^2(\xi), \tag{2.5}$$

where the auxiliary function $R(\xi)$ satisfies the Riccati equation

$$R'(\xi) = B_0 + B_1 R(\xi) + B_2 R^2(\xi). \tag{2.6}$$

Substitution of (2.5) and (2.6) into (2.4) leads to an algebraic system whose regular solitary-wave branch is characterized by

$$A_1 = 0, \quad A_0 = -\frac{b}{d}, \quad A_2 = -\frac{6aB_2^2}{d}, \quad 8aB_0B_2 = b. \tag{2.7}$$

Selecting the hyperbolic Riccati branch

$$R(\xi) = -\sqrt{m}\tanh(\sqrt{m}(\xi - \xi_0)), \quad m = \frac{c - \alpha k - \beta\ell}{4\mu c(k^2 + \ell^2)}, \tag{2.8}$$

we obtain, after simplification, the exact solitary-wave solution

$$u_{\mathrm{ex}}(x, y, t) = \frac{3(c - \alpha k - \beta\ell)}{\gamma k + \delta\ell} \operatorname{sech}^2\left[\frac{1}{2}\sqrt{\frac{c - \alpha k - \beta\ell}{\mu c(k^2 + \ell^2)}}(kx + \ell y - ct - \xi_0)\right]. \tag{2.9}$$

This expression represents a smooth regular solitary-wave solution.

This solution exists provided that

$$\gamma k + \delta\ell \neq 0, \quad \frac{c - \alpha k - \beta\ell}{\mu c(k^2 + \ell^2)} > 0. \tag{2.10}$$

For all closed-form travelling-wave solutions below, the parameters are chosen so that the denominators do not vanish. They are also chosen so that the square roots are real when real-valued wave profiles are considered. Thus, we require

$$\gamma k + \delta\ell \neq 0, \quad c \neq 0, \quad k^2 + \ell^2 \neq 0.$$

For the hyperbolic branches (2.9) and (2.11), we assume

$$\frac{c - \alpha k - \beta\ell}{\mu c(k^2 + \ell^2)} > 0.$$

For the trigonometric branches (2.12) and (2.13), we assume

$$\frac{\alpha k + \beta\ell - c}{\mu c(k^2 + \ell^2)} > 0.$$

The singular branches are used only away from their singular points. In particular, Eqs (2.11)–(2.13) are restricted away from the zeros of the corresponding sinh, cos, and sin factors, respectively.

Equation (2.9) describes a smooth, spatially localized solitary pulse that propagates obliquely in the (x, y)-plane without losing its shape, amplitude, or speed. This solitary pulse is the main analytical standard against which all subsequent numerical experiments are compared.

The same Riccati framework also produces singular and periodic branches. Specifically, the hyperbolic coth branch leads to the singular hyperbolic solution as follows:

$$u_{\mathrm{ex},1}(x, y, t) = \frac{3(\alpha k + \beta \ell - c)}{\gamma k + \delta \ell} \operatorname{csch}^2\left[\frac{1}{2}\sqrt{\frac{c - \alpha k - \beta \ell}{\mu c(k^2 + \ell^2)}}(kx + \ell y - ct - \xi_0)\right]. \tag{2.11}$$

This expression represents a singular hyperbolic travelling-wave solution, whereas the trigonometric branches lead to periodic solutions as follows:

$$u_{\mathrm{per},1}(x, y, t) = -\frac{3(\alpha k + \beta \ell - c)}{\gamma k + \delta \ell} \sec^2\left[\frac{1}{2}\sqrt{\frac{\alpha k + \beta \ell - c}{\mu c(k^2 + \ell^2)}}(kx + \ell y - ct - \xi_0)\right]. \tag{2.12}$$

This expression represents a periodic trigonometric travelling-wave solution and

$$u_{\mathrm{per},2}(x, y, t) = -\frac{3(\alpha k + \beta \ell - c)}{\gamma k + \delta \ell} \csc^2\left[\frac{1}{2}\sqrt{\frac{\alpha k + \beta \ell - c}{\mu c(k^2 + \ell^2)}}(kx + \ell y - ct - \xi_0)\right]. \tag{2.13}$$

This expression represents a singular periodic travelling-wave solution.

These auxiliary branches are of analytical interest, but they are not suitable as primary numerical benchmarks because of their singular structure. For verification purposes, the localized wave (2.9) is the most relevant exact solution.

2.3. Generalized Arnous-type representation

For completeness, we briefly indicate that the reduced RLW Eq (2.4) can also be treated within a generalized Arnous-type framework [17].

The generalized Arnous-type representation in (2.14) is also based on a finite expansion principle. In this framework, the ratio $\Phi'(\xi)/\Phi(\xi)$ is used as the auxiliary building block, and the quadratic order is again selected by balancing the highest derivative term with the quadratic nonlinearity in (2.2). The auxiliary relation in Eq (2.17) generates hyperbolic, trigonometric, and singular branches depending on the parameter choices. In the present paper, we record the branches that are relevant for constructing explicit travelling-wave benchmark profiles for the adaptive numerical tests.

In this representation, one seeks

$$U(\xi) = \alpha_0 + \alpha_1 \frac{\Phi'(\xi)}{\Phi(\xi)} + \beta_1 \left(\frac{\Phi'(\xi)}{\Phi(\xi)}\right)^2, \tag{2.14}$$

where the auxiliary function $\Phi(\xi)$ satisfies

$$(\Phi'(\xi))^2 = (\Phi^2(\xi) - \chi)\sigma^2. \tag{2.15}$$

Substitution of (2.14) and (2.15) into (2.4) yields an algebraic compatibility system whose regular hyperbolic branch reproduces the same localized solitary-wave solution already obtained by the Riccati

approach, namely,

$$u_{\mathrm{ex}}(x,y,t) = \frac{3(c-\alpha k-\beta\ell)}{\gamma k+\delta\ell}\,\mathrm{sech}^2\left[\frac{1}{2}\sqrt{\frac{c-\alpha k-\beta\ell}{\mu c(k^2+\ell^2)}}(kx+\ell y-ct-\xi_0)\right]. \tag{2.16}$$

Likewise, singular and periodic branches may be recovered in the forms

$$u_{\mathrm{ex},1}(x,y,t) = \frac{3(\alpha k+\beta\ell-c)}{\gamma k+\delta\ell}\,\mathrm{csch}^2\left[\frac{1}{2}\sqrt{\frac{c-\alpha k-\beta\ell}{\mu c(k^2+\ell^2)}}(kx+\ell y-ct-\xi_0)\right] \tag{2.17}$$

and

$$u_{\mathrm{per}}(x,y,t) = -\frac{3(\alpha k+\beta\ell-c)}{\gamma k+\delta\ell}\,\mathrm{sec}^2\left[\frac{1}{2}\sqrt{\frac{\alpha k+\beta\ell-c}{\mu c(k^2+\ell^2)}}(kx+\ell y-ct-\xi_0)\right], \tag{2.18}$$

with analogous csc^2-type periodic variants. Nevertheless, for the present RLW reduction, the Riccati formulation remains algebraically more direct and is therefore adopted as the principal exact-solution route.

2.4. Exact auxiliary variable in the mixed formulation

For consistency with the mixed formulation used in the numerical section, we define the auxiliary variable by

$$v = u - \mu\left(u_{xx}+u_{yy}\right). \tag{2.19}$$

Under the travelling-wave reduction (2.1), one has

$$u_{xx}+u_{yy} = (k^2+\ell^2)U''(\xi),$$

so that

$$v = U - \mu(k^2+\ell^2)U''. \tag{2.20}$$

Using the reduced Eq (2.2), this can be written in closed form as

$$v = \frac{\alpha k+\beta\ell}{c}\,U + \frac{\gamma k+\delta\ell}{2c}\,U^2. \tag{2.21}$$

Hence, in terms of the exact solitary-wave benchmark (2.9), the associated auxiliary field is

$$v_{\mathrm{ex}}(x,y,t) = \frac{\alpha k+\beta\ell}{c}\,u_{\mathrm{ex}}(x,y,t) + \frac{\gamma k+\delta\ell}{2c}\,u_{\mathrm{ex}}^2(x,y,t). \tag{2.22}$$

This explicit formula is fully consistent with the mixed representation adopted later for the adaptive semi-discretization.

2.5. *Exact initial and boundary data*

The exact travelling-wave solution (2.9) provides a rigorous analytical benchmark for the present RLW model. The initial and boundary data for the later numerical study are therefore generated directly from the exact pair

$$(u_{\mathrm{ex}}(x, y, t),\ v_{\mathrm{ex}}(x, y, t)).$$

Accordingly, the initial conditions are taken as

$$u_0(x, y) = u_{\mathrm{ex}}(x, y, 0), \quad v_0(x, y) = v_{\mathrm{ex}}(x, y, 0), \quad (x, y) \in \Omega, \tag{2.23}$$

while the Dirichlet boundary data on $\partial\Omega$ are prescribed by

$$u(x, y, t) = u_{\mathrm{ex}}(x, y, t), \quad (x, y) \in \partial\Omega, \quad t \in [0, T]. \tag{2.24}$$

The solitary-wave solution (2.9) represents a smooth, localized travelling profile that is free of singularities and preserves its shape during propagation. This makes it an ideal reference solution for assessing numerical accuracy, wave profile preservation, and the effectiveness of adaptive mesh concentration inside regions of strong gradients. Consequently, the exact pair (u, v) provides a consistent and reliable benchmark for testing the proposed adaptive framework.

The analytical construction of the two-dimensional RLW model is shown in Figure 1 for $u(x, y, t)$. The upper panels are given by (2.16) and the lower panels are given by the auxiliary variable $v(x, y, t)$ in (2.22).

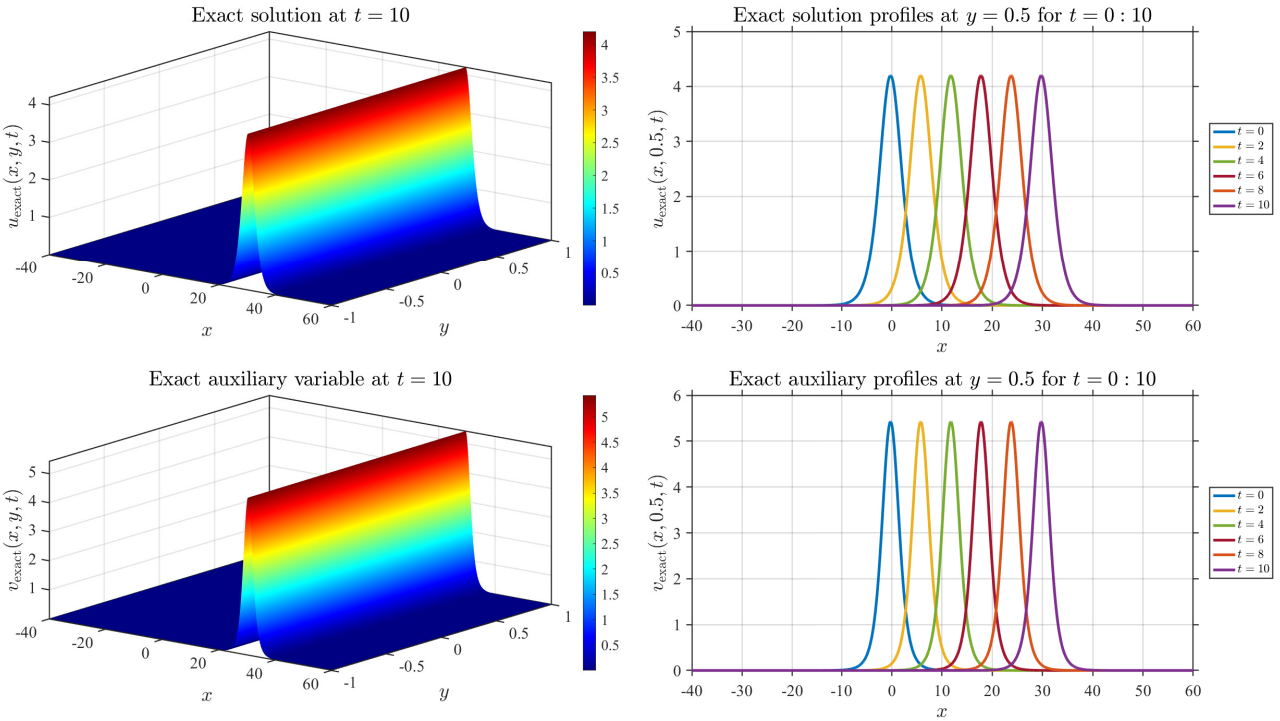

Figure 1. Two-dimensional RLW model: exact solution $u(x, y, t)$ and auxiliary field $v(x, y, t)$. Left panels: three-dimensional surfaces at $t = 10$; Right panels: one-dimensional profiles at $y = 0.5$ for selected time levels.

The plots of u illustrate a localized travelling wave that moves in the (x, y)-plane at an oblique angle to itself. The travelling wave moves in the (x, y)-plane while maintaining its shape. The aforementioned behavior reflects the RLW wave, which preserves its shape and does not deform rapidly. The plots of v are in the same propagation direction and same localization as u, except that they are in a region of lower amplitude because of their mixed definition. The mixed definition of v is a linear contribution that is proportional to u and a quadratic nonlinear correction. Hence, v is an auxiliary wave that is a regularized wave quantity that holds additional information about the dispersive nonlinear structure. From the perspective of numerical analysis, the figure validates that the exact pair (u, v) continues to remain smooth, structured, and compatible throughout the various stages of propagation. This allows for a dense benchmark in terms of testing the accuracy, profile preservation, and adaptive mesh concentration for the main wave region.

All obtained travelling-wave expressions were verified by direct symbolic substitution into the governing RLW equation using Mathematica. In each case, the residual was simplified under the stated parameter restrictions and reduced identically to zero.

Although these additional branches enrich the analytical structure of the model, the regular solitary-wave branch is the most appropriate benchmark for the adaptive numerical tests because it remains smooth and permits reliable quantitative error measurement.

3. Adaptive mixed RLW discretization and numerical framework

In this section, we elaborate on the adaptive numerical framework implemented for the two-dimensional RLW equation. We introduce the mixed PMA-based semi-discretization on bidirectionally adaptive nonuniform tensor-product grids and address stability, consistency, convergence, and computational realisation. Recent analytical-computational approaches have demonstrated that adaptive mesh redistribution is especially effective for nonlinear dispersive systems that have dominant structures remaining localized or forming strong gradients. Specifically, PMA- and moving-mesh-based approaches have been successfully utilized for generalized breaking soliton models and improved Boussinesq-type equations, for which adaptive redistribution significantly improved local resolution and numerical efficiency in comparison to uniform discretizations [15, 16]. This motivates the current bidirectional adaptive scheme to the two-dimensional RLW equation.

3.1. PMA-based semi-discretization for the two-dimensional RLW equation

The adaptive numerical framework is developed for the governing two-dimensional RLW equation introduced in Eq (1.1).

For adaptive computation, it is convenient to rewrite Eq (1.1) in the mixed form

$$v = u - \mu\left(u_{xx} + u_{yy}\right), \quad v_t + \alpha u_x + \beta u_y + \gamma u\, u_x + \delta u\, u_y = 0. \tag{3.1}$$

This representation separates the transport-dominated nonlinear evolution from the elliptic regularization and leads naturally to a differential-algebraic formulation on each frozen adaptive mesh. In the present implementation, the moving mesh is realized on a tensor-product family of nonuniform physical grids,

$$x_1(t) < x_2(t) < \cdots < x_{N_x}(t), \quad y_1(t) < y_2(t) < \cdots < y_{N_y}(t),$$

which are updated by rezoning in both spatial directions. Let $U_h(t)$ and $V_h(t)$ denote the nodal vectors associated with u and v, respectively, on the current grid. For each frozen mesh, the one-dimensional first- and second-derivative matrices in the x- and y-directions are constructed from five-point Fornberg finite-difference weights on the current nonuniform nodes. Denoting these by

$$D_x, \quad D_{xx} \in \mathbb{R}^{N_x \times N_x}, \quad D_y, \quad D_{yy} \in \mathbb{R}^{N_y \times N_y},$$

the corresponding two-dimensional discrete operators are assembled through Kronecker products as

$$D_x^h = I_{N_y} \otimes D_x, \quad D_{xx}^h = I_{N_y} \otimes D_{xx}, \quad D_y^h = D_y \otimes I_{N_x}, \quad D_{yy}^h = D_y^{(2)} \otimes I_{N_x}, \tag{3.2}$$

where I_{N_x} and I_{N_y} are identity matrices of the indicated sizes, and $D_y^{(2)} \equiv D_{yy}$. The discrete convection operator is then written as

$$\mathcal{N}_h(U_h) = \alpha D_x^h U_h + \beta D_y^h U_h + \gamma U_h \circ D_x^h U_h + \delta U_h \circ D_y^h U_h, \tag{3.3}$$

where $\circ$ denotes componentwise multiplication. The algebraic regularization is discretized directly on the same nonuniform tensor grid by

$$V_h = U_h - \mu(D_{xx}^h + D_{yy}^h)U_h. \tag{3.4}$$

Accordingly, on each frozen mesh, the mixed semi-discretization takes the differential–algebraic form

$$\frac{d}{dt}V_h + \mathcal{N}_h(U_h) = 0, \qquad V_h - U_h + \mu(D_{xx}^h + D_{yy}^h)U_h = 0. \tag{3.5}$$

In the actual computation, Dirichlet boundary values are imposed strongly from the prescribed benchmark profile, so that only the interior nodal values enter the implicit DA solve. The resulting index-one system is advanced on each time slab by `ode15i`, with a consistency correction supplied by `decic` whenever needed. The adaptive redistribution is performed within a PMA/rezoning framework in which the two one-dimensional meshes are regenerated separately from directional monitor densities extracted from the current numerical field. Specifically, if $U = (U_{ij})$ denotes the grid function on the current tensor mesh, then the directional indicators are defined by

$$g_{x,1}(i) = \left(\frac{1}{N_y} \sum_{j=1}^{N_y} \left[(D_x U)_{ij} \right]^2 \right)^{1/2}, \quad g_{x,2}(i) = \left(\frac{1}{N_y} \sum_{j=1}^{N_y} \left[(D_{xx} U)_{ij} \right]^2 \right)^{1/2}, \tag{3.6}$$

and analogously,

$$g_{y,1}(j) = \left(\frac{1}{N_x} \sum_{i=1}^{N_x} \left[(U D_y^\top)_{ij} \right]^2 \right)^{1/2}, \quad g_{y,2}(j) = \left(\frac{1}{N_x} \sum_{i=1}^{N_x} \left[(U D_{yy}^\top)_{ij} \right]^2 \right)^{1/2}. \tag{3.7}$$

After normalization, these indicators generate monitor densities of arc-length, curvature, or hybrid type. In compact form,

$$\rho_{\mathrm{arc}} = (1 + \alpha_{\mathrm{arc}}\, g_1^2)^{p_{\mathrm{arc}}}, \tag{3.8}$$

$$\rho_{\mathrm{curv}} = (1 + \alpha_{\mathrm{curv}} \sqrt{g_2 + \varepsilon})^{p_{\mathrm{curv}}}, \tag{3.9}$$

and

$$\rho_{\mathrm{hyb}} = (1 + w_1 g_1 + w_2 \sqrt{g_2 + \varepsilon})^{p_{\mathrm{hyb}}}, \tag{3.10}$$

where g_1 and g_2 denote the normalized first- and second-derivative indicators in the relevant coordinate direction. The new meshes are then obtained by directional equidistribution after smoothing, capping, blending with a uniform reference distribution, and enforcing lower bounds on admissible cell widths together with upper bounds on neighboring mesh ratios. At the end of each time slab, the numerical solution is transferred from the old tensor grid to the new one by shape-preserving tensor-product p-chip interpolation, the boundary data are reimposed, and the auxiliary variable is reconstructed from (3.4). This solve–rezone–interpolate–reconstruct sequence constitutes one complete adaptive PMA cycle for the two-dimensional RLW equation. Such a rezoning philosophy is consistent with recent work on adaptive nonlinear oscillatory systems, where dynamic node relocation raised accuracy in the vicinity of steep or interacting structures while continuing a reasonably uniform mesh and computational efficiency [15, 16].

3.2. Stability of the adaptive semi-discrete formulation

The stability of the present method is most naturally interpreted in the admissible-mesh regime. More precisely, we assume that for every frozen adaptive mesh, there exist positive constants

$$\underline{h}_x,\ \underline{h}_y,\ \overline{h}_x,\ \overline{h}_y$$

such that

$$0 < \underline{h}_x \le x_{i+1} - x_i \le \overline{h}_x, \quad 0 < \underline{h}_y \le y_{j+1} - y_j \le \overline{h}_y, \tag{3.11}$$

together with uniform bounds on the ratios of neighboring cell widths.

These criteria guarantee that the tensor grid is one-to-one, has smooth gradation, and is free of pathological compression and loss of resolution. Given this admissibility assumption, the discrete regularizing operator

$$M_h := I - \mu(D^h_{xx} + D^h_{yy}) \tag{3.12}$$

remains uniformly well-posed for each frozen mesh. Therefore, the discrete algebraic relation (3.4) determines U_h from V_h stably, and the semi-discrete system (3.5) is locally well-posed as an index-one DA. Linearization about the bounded reference state $\bar{U}_h$ gives

$$M_h \frac{d}{dt} e_h + A_h(\bar{U}_h) e_h = 0, \tag{3.13}$$

where e_h is the perturbation and $A_h(\bar{U}_h)$ is the Jacobian of the discrete convection operator. Since the discrete first-derivative operators are built from centered local formulas, the leading transport contribution is non-dissipative at the main order, while the other variable-coefficient terms are bounded by the reference solution's boundedness along with the mesh regularity constants.

Under the admissibility assumptions, the linearized frozen-mesh system formally satisfies an estimate of the form

$$\|e_h(t)\|_{M_h} \le \exp(Ct)\, \|e_h(0)\|_{M_h}, \tag{3.14}$$

where C is a function of the solution amplitude, the nonlinear coefficients, and the admissible mesh constants, but not the mesh resolution. This indicates conditional stability of the frozen-mesh semi-discrete approximation.

The fully adaptive algorithm alternates frozen-mesh DA solves with rezoning steps, so the overall stability statement must also account for the mesh update. In the present implementation, admissibility is enforced numerically through repeated monitor smoothing, density capping, blending with a uniform mesh, lower bounds on the cell widths in both directions, upper bounds on neighboring mesh ratios, and shape-preserving transfer between successive meshes. The appropriate stability interpretation is therefore *conditional stability under admissible bidirectional mesh evolution*, which is both mathematically defensible and consistent with the actual solver.

3.3. Consistency and convergence

On each frozen admissible tensor-product mesh, the discrete operators in (3.2) are consistent approximations to the corresponding physical derivatives. Assuming that the exact solution is sufficiently smooth and that the mesh remains smoothly graded, one has the estimates

$$u_x - D_x^h u = O(h_x^2 + h_y^2), \quad u_y - D_y^h u = O(h_x^2 + h_y^2), \tag{3.15}$$

together with

$$(u_{xx} + u_{yy}) - (D_{xx}^h + D_{yy}^h)u = O(h_x^2 + h_y^2), \tag{3.16}$$

where $h_x = \max_i(x_{i+1} - x_i)$ and $h_y = \max_j(y_{j+1} - y_j)$. Hence the frozen-mesh mixed semi-discretization is formally second-order consistent in space.

For the complete adaptive algorithm, however, one additional mechanism must be taken into account, namely, the rezoning transfer between successive meshes. After each mesh update, the numerical solution is interpolated from the old tensor grid to the new one by tensor-product p-chip interpolation. This transfer is robust and shape-preserving, but it introduces an additional error contribution that is not part of the local differential truncation error on a frozen mesh.

Consequently, although the differential operators themselves are spatially second-order consistent, the global convergence behavior of the complete adaptive rezoning algorithm should be interpreted with appropriate caution. The observed convergence of the fully adaptive method is therefore empirical and reflects the combined effects of differential approximation, mesh redistribution, and inter-mesh transfer between successive adaptive meshes.

This understanding is also consistent with recent adaptive wave studies, where the observed convergence relies on multiple factors beyond the differential approximation, including mesh redistribution and the transfer of the solution across successive grids [14, 15].

When the mesh updates remain sufficiently mild and the solution structure is smooth, near-second-order behavior may still be observed. When the rezoning transfer becomes dominant, the measured order may deteriorate even though the adaptive mesh continues to provide substantially improved local resolution of the relevant wave structures. In the present study, the convergence assessment is carried out by direct comparison with a prescribed benchmark field u_{ref}. In the single-wave configuration, u_{ref} coincides with the exact travelling-wave solution. In the two-pulse configuration, u_{ref} denotes the prescribed reference state used to test the adaptive method under a richer multi-structure evolution. At

the final time T, the numerical error is measured by

$$E_{L^2} = \left(\sum_{i=1}^{N_x} \sum_{j=1}^{N_y} |U_{ij} - u_{\text{ref}}(x_i, y_j, T)|^2 \, \omega_i^x \, \omega_j^y \right)^{1/2} \tag{3.17}$$

and

$$E_{L^\infty} = \max_{1 \le i \le N_x,\ 1 \le j \le N_y} |U_{ij} - u_{\text{ref}}(x_i, y_j, T)|, \tag{3.18}$$

where ω_i^x and ω_j^y are the one-dimensional trapezoidal weights on the current adaptive meshes in the x- and y-directions, respectively. In addition, the algebraic consistency of the mixed formulation is monitored through

$$R_{\text{alg}} = V_h - U_h + \mu(D_{xx}^h + D_{yy}^h)U_h. \tag{3.19}$$

For a sequence of refined grids, the experimental orders of convergence are estimated by

$$\text{EOC}_{L^2} = \frac{\log\left(E_{L^2}^{(m)} / E_{L^2}^{(m+1)}\right)}{\log 2}, \quad \text{EOC}_{L^\infty} = \frac{\log\left(E_{L^\infty}^{(m)} / E_{L^\infty}^{(m+1)}\right)}{\log 2}. \tag{3.20}$$

3.4. Computational realization of the generalized adaptive mixed RLW discretization

The computational implementation of the current solver comprises a generalized adaptive verification framework in which the analytical model, benchmark data, and numerical model remain functionally coupled for the whole duration of the simulation. Instead of advancing the first RLW equation directly in its mixed space time configuration, the implementation evolves the set of auxiliary variables in the equations in a stepwise manner on a series of frozen non-uniform tensor grids and performs spatial rezoning in both directions. A notable advantage of the solver is its two-tier benchmark provision, selectable via the parameter `icType`. The first configuration is the exact solution for a single travelling solitary wave,

$$u(x, y, t) = A, \operatorname{sech}^2(B(kx + \ell y - ct - \xi_0)), \tag{3.21}$$

which serves as the default verification benchmark on

$$(N_x, N_y) = (121, 61), \quad (x, y) \in [-40, 60] \times [-1, 1], \quad t \in \{0, 2, 4, 6, 8, 10\}.$$

For this case, the default parameter set is

$$\alpha = 1, \quad \beta = 0.5, \quad \gamma = 1, \quad \delta = 0.5, \quad \mu = 1, \quad k = 1, \quad \ell = 0.5, \quad c = 3, \quad \xi_0 = 0,$$

with

$$A = \frac{3(c - \alpha k - \beta \ell)}{\gamma k + \delta \ell}, \quad B = \frac{1}{2} \sqrt{\frac{c - \alpha k - \beta \ell}{\mu c (k^2 + \ell^2)}}.$$

The second configuration is a two-pulse reference state,

$$u(x, y, t) = \sum_{j=1}^{2} 3c_j \operatorname{sech}^2(k_j(x + y - v_j t - x_j - y_j)), \quad k_j = \frac{1}{2} \sqrt{\frac{c_j}{1 + c_j}}, \quad v_j = 2(1 + c_j), \tag{3.22}$$

used to probe the adaptive method in a richer multi-structure regime. Its default computational setting is

$$(N_x, N_y) = (121, 121), \quad (x, y) \in [0, 120] \times [0, 120], \quad t \in \{0, 5, 10, 15\},$$

with

$$\alpha = \beta = \gamma = \delta = \mu = 1, \quad (c_1, c_2) = (0.2, 0.4), \quad (x_1, y_1) = (35, 35), \quad (x_2, y_2) = (55, 55).$$

The numerical assessment is broad for this dual benchmark configuration. The first case is a simple verification test with a travelling wave. The second case analyses the performance of the adaptive algorithm for resolving several coupled localized structures in the same computational domain. The simulation starts with a uniform mesh and, prior to the first calculation step, this mesh is adjusted to fit the required initial configuration. Thereafter, for each time slab $[t_n, t_{n+1}]$, the mixed RLW system is integrated on the current frozen tensor grid by `ode15i`. To guarantee algebraic compatibility at the beginning of each slab, the initial state is checked against the DA residual and, whenever needed, corrected by a `decic`-based consistency step. In addition, the sparsity pattern of the Jacobian with respect to both the state vector and its time derivative is supplied explicitly to the integrator, which improves robustness and reduces the cost of the implicit solve. Mesh redistribution is driven by directional monitor densities in both x and y. The implementation allows three monitor choices, namely, arc-length, curvature, and hybrid forms, with the hybrid monitor used by default. In the default parameter set,

$$\alpha_{\text{arc}} = 7, \quad p_{\text{arc}} = 1,$$

$$\alpha_{\text{curv}} = 2, \quad p_{\text{curv}} = 0.85,$$

and

$$w_1 = 2.3, \quad w_2 = 0.45, \quad p_{\text{hyb}} = 1.05.$$

The monitor densities are regularized by four smoothing passes, capped by a density factor of 5, and blended with a uniform reference distribution using a relaxation parameter equal to 0.10. Additional geometric safeguards are imposed through lower spacing thresholds

$$\Delta x_{\min} = 0.08\,\frac{x_{\max} - x_{\min}}{N_x - 1}, \quad \Delta y_{\min} = 0.08\,\frac{y_{\max} - y_{\min}}{N_y - 1},$$

together with neighboring-cell ratio bounds

$$\frac{\Delta x_{i+1}}{\Delta x_i} \le 1.18, \quad \frac{\Delta y_{j+1}}{\Delta y_j} \le 1.18.$$

These devices enable the moving mesh to react to the different features of the numerical solution, both with sensitivity and with restraint. Specifically, the grid moves to areas of larger gradients and greater curvature, where greater refinement is warranted. Conversely, limits are imposed to restrain excessive clustering or discontinuities in mesh density, preserving computational stability. Upon the acceptance of the updated mesh, the numerical solution is migrated from the old tensor grid to the new one via shape-preserving tensor-product (p)-chip interpolation, the benchmark boundary conditions are reimposed, and the auxiliary variable is reconstructed from (3.4). This solve-rezone-interpolate-reconstruct cycle constitutes an adaptive PMA step. The main effect is that

steep features are accompanied by dense local node distributions, smooth areas are resolved in an economical way, and the mixed RLW dynamics are solved on a mesh that continuously reorganizes itself to the evolving features of the solution.

Finally, the implementation is equipped with a systematic diagnostics and verification layer. At every requested output time, the code stores the current adaptive meshes, the numerical field, the benchmark field, and the corresponding pointwise error. The global discrepancy is monitored through discrete L^2 and L^∞ error measures evaluated directly on the adaptive mesh, while additional indicators such as the minimum and maximum mesh widths in both directions are reported during the computation. The solver also produces publication-quality visualizations of the numerical wave surface, the adaptive mesh, and the temporal history of the error norms. Accordingly, the present implementation should be viewed not merely as a computational routine, but as a generalized, fully two-dimensional, adaptive verification environment for the RLW equation within a unified DA–PMA framework.

4. Results and discussion

This section presents the numerical evidence supporting the adaptive mixed RLW framework developed in the preceding sections. The discussion is organized around two complementary benchmark settings. The first is the exact single solitary wave (3.21), which offers an unambiguous way to verify how well our method converges, preserves the wave, and keeps the wave shape with a focused mesh. The second, the two pulse case (3.22), assesses how well the PMA strategy works in more complicated cases. Combined, these cases demonstrate that the method is consistent and resolves local waves on a moving nonuniform mesh.

The initial conditions, boundary values, and auxiliary-field data used in the numerical experiments are obtained directly from the benchmark travelling-wave solutions derived in Section 2. This construction ensures consistency between the analytical benchmark profiles and the adaptive numerical framework throughout the computations and allows accurate quantitative error assessment against the exact reference solutions.

Convergence study for the single-wave benchmark. A grid-refinement comparison between the PMA-based adaptive solver and the uniform, fixed mesh solver shows that the PMA adaptive solver is more effective. In addition, the adaptive strategy shows that the PMA redistributes the mesh, leading to significant reductions in the error levels.

In Table 2, N denotes the effective one-dimensional refinement level used for the grid-refinement study. For the two-dimensional experiments, the corresponding spatial degrees of freedom are chosen so that the adaptive and fixed-mesh computations use comparable tensor-product resolutions at each refinement level. The fixed-mesh method uses the same mixed differential–algebraic formulation, the same Fornberg finite-difference discretization, the same boundary data, and the same implicit time integrator as the adaptive method. The only difference is that the fixed-mesh computation is performed without PMA-based rezoning and without inter-mesh redistribution. The comparison therefore isolates the effect of adaptive mesh redistribution. It does not reflect changes in the underlying spatial discretization or time integration. Table 2 shows the error comparison between the two methods. Here, N is the effective one-dimensional refinement level.

Table 2. Error comparison between the adaptive and fixed-mesh methods.

N	PMA		Fixed mesh	
	L^2 error	L^∞ error	L^2 error	L^∞ error
30	1.62E-1	6.09E-2	5.86E-0	2.28E-0
60	3.44E-2	1.04E-2	2.57E-0	6.94E-1
120	1.09E-2	2.51E-3	4.34E-1	1.02E-1
240	1.05E-3	5.08E-4	7.86E-2	4.75E-2
480	2.34E-4	5.66E-5	2.01E-2	1.83E-2
960	5.06E-6	1.23E-6	5.76E-3	2.88E-3

Table 2 shows that the PMA-based adaptive strategy outperforms the uniform fixed-mesh adaptive strategy. Even on coarse and moderate grids, the adaptive method results in a significant error reduction in both L^2 and L^∞ norms. This proves that mesh redistribution results in improved performance by increasing spatial resolution in the dominant section of the solitary wave, as opposed to an even distribution of the nodes throughout the entire mesh. Table 2 confirms that the PMA method optimally reallocates a fixed spatial resolution into an improved approximative quality. In the localized RLW wave structures, the typical numerical error is concentrated at the propagating core. A uniform grid will splay resolution that is instead used to correct the wave into inactive portions of the grid, across the wave. In the PMA method, the nodes are instead directed to the core region of the wave. This advantage is reflected in both error measures as the wave is locally refined. The adaptive computations were also tested under several variations of the monitor parameters, including changes in the monitor intensity, smoothing level, and redistribution blending factors. The numerical results showed that the overall wave-resolution behavior and the qualitative mesh adaptation pattern remained stable across a moderate range of parameter choices. Larger monitor intensities produced stronger mesh concentration near the dominant wave structures, while excessive concentration occasionally reduced global smoothness of the mesh trajectories. In the present computations, the selected monitor parameters provided a balanced compromise between local wave resolution, mesh regularity, and numerical robustness.

Figure 2 provides a visual representation of the convergence behavior reported in Table 2. The log-log plots demonstrate the decay of the numerical errors under grid refinement for both the PMA-based adaptive computation and the corresponding fixed-mesh discretization. The adaptive framework consistently produces smaller errors in both the global L^2 norm and the local L^∞ norm. The reference $O(N^{-2})$ curves indicate that the observed behavior is consistent with the expected second-order spatial approximation on frozen meshes. The adaptive redistribution improves the effective use of the available spatial resolution by concentrating mesh points near the dominant wave regions instead of distributing them uniformly throughout the computational domain. Consequently, the PMA-based strategy captures the localized wave structure more efficiently and achieves improved numerical accuracy with the same effective spatial resolution. The convergence behaviour of both numerical strategies is illustrated in Figure 2.

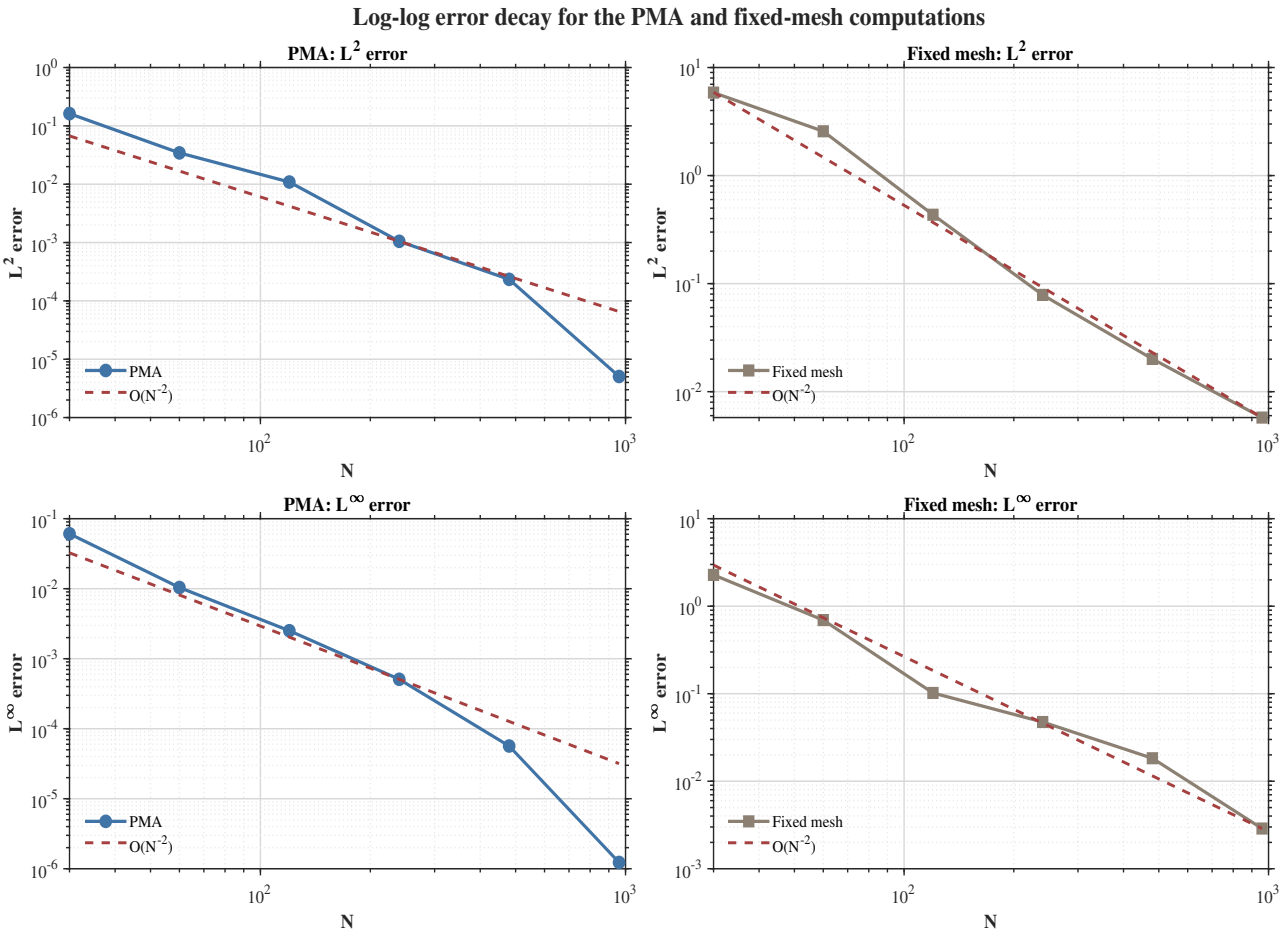

Figure 2. Log-log decay of the discrete L^2 and L^∞ errors for the PMA-based adaptive computation and the corresponding fixed-mesh discretization in the single-wave benchmark. The reference $O(N^{-2})$ trends are included for comparison.

Figure 3 shows the numerical evolution and adaptive meshes at times $t = 2$, $t = 6$, and $t = 10$. These times provide a good description of the wave propagation in the interval. The RLW profiles at the times given and at the dominant wave structure are clear of spurious deformations. This is proof that the adaptive mixed discretization was stable and maintained accuracy to that point in time. The given meshes show that the PMA redistribution remains concentrated around the dominant regions. This is evidence of the adaptive spatial configuration error levels. Although the solution surfaces in Figure 3 appear visually similar, the main difference between the subplots is the spatial translation of the solitary structure and the corresponding redistribution of the adaptive mesh. This behavior is expected for a travelling solitary wave, since the benchmark profile propagates while preserving its amplitude and shape. Therefore, the similarity of the solution surfaces is not a lack of dynamics, but rather evidence that the numerical method preserves the coherent travelling-wave profile. The adaptive meshes, however, show the movement of the concentrated grid region as it follows the dominant wave core from one time level to another.

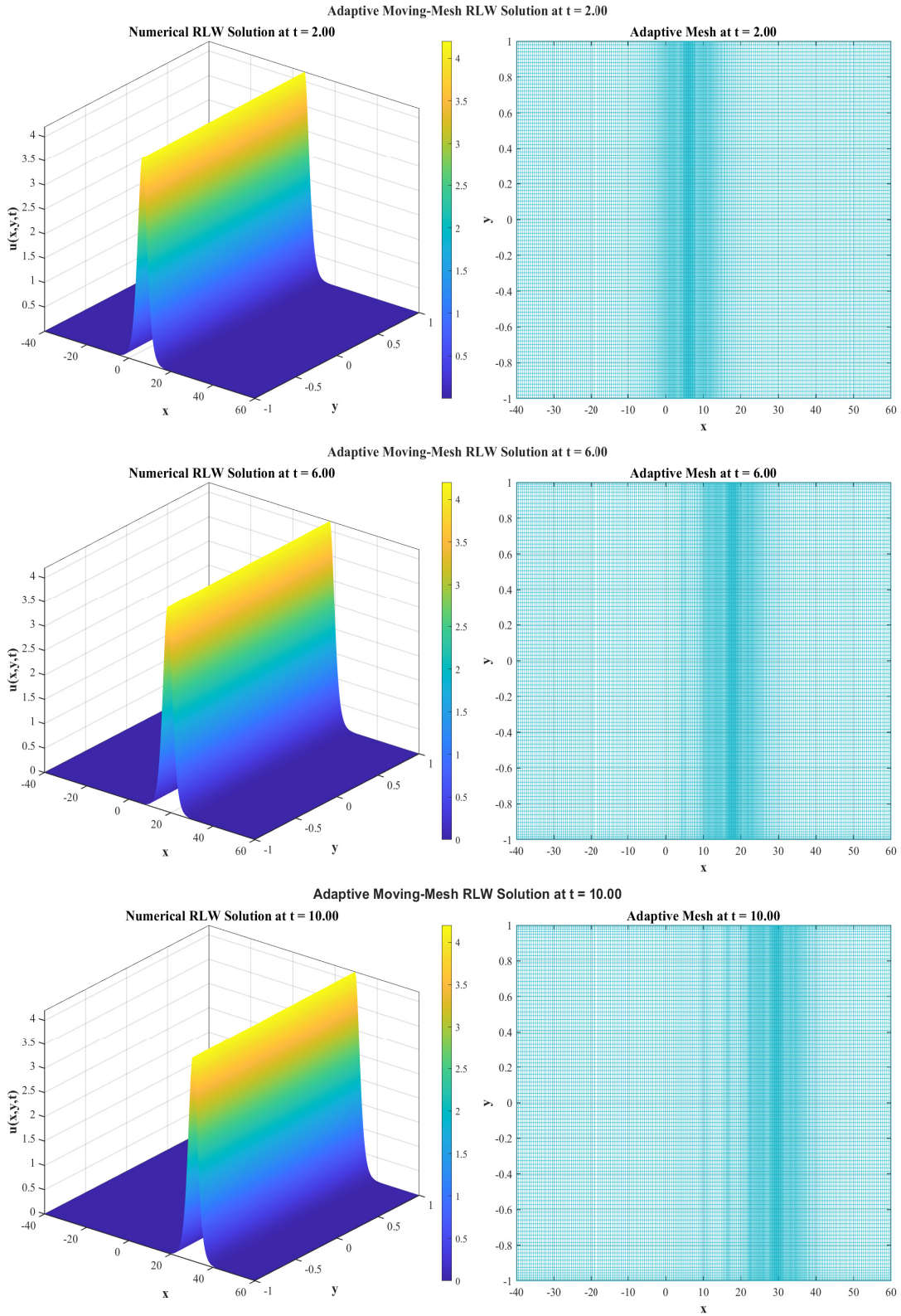

Figure 3. Adaptive evolution of single solitary wave (3.21) at times: $t = 2$; $t = 6$; $t = 10$. Each figure shows the numerical solution and respective adaptive mesh.

Figure 4 offers a complementary perspective of one of the adaptive computations associated with the single solitary wave (3.21). The left side illustrates mesh mapping of $x(\xi, t)$ at multiple representative times, providing clarity on the dynamic redistribution of grid points as the solitary structure traverses the computational domain. The nonuniform deformation of the mapping reflects the adaptive strategy of continuously shifting the focus of its resolution to the wave core, as opposed to keeping a uniformly distributed focus throughout the structure. Such behavior is entirely consistent with the goal of the PMA mechanism, which is to position the mesh density on the solution's dynamically and geometrically active components. The right side of the figure aims to show the corresponding effect on the numerical approximation. The numerical profiles reported at each of the time levels appear to be in close proximity to the solution of the travelling wave on the approximation, demonstrating that the adaptive mixed discretization is capable of excellent benchmark approximation in the structure to be solved. This figure is meaningful from a numerical analysis perspective as it captures the two properties in one image—the first being that the mesh movement is physically justifiable and is concentrated around the localized wave region, and the second being that the adaptive redistribution is able to retain the profile with minimal changes over time. Therefore, this figure is an excellent visual explanation of the reduced error levels and improved convergence behavior demonstrated previously with the PMA-based adaptive solver.

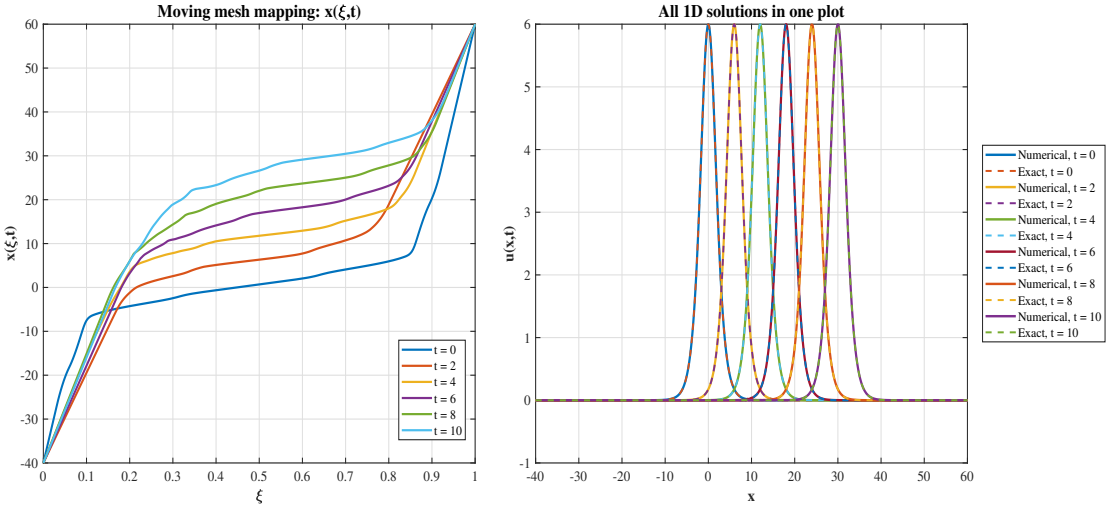

Figure 4. One-dimensional diagnostics for the single solitary wave (3.21). Left: moving-mesh mapping $x(\xi, t)$; Right: numerical and exact profiles at selected time levels.

It is worth noting that the peak amplitude recorded in the one-dimensional diagnostics surpasses the oblique two-dimensional benchmark mentioned earlier; this is not a contradiction in the numbers. In fact, the one-dimensional outcomes are derived from the simplified RLW model obtained by eliminating the transverse contribution, specifically by setting $y = 0$, $u_y = 0$, and $u_{yy} = 0$. Consequently, the corresponding travelling-wave amplitude is

$$A_{1D} = \frac{3(c - \alpha k)}{\gamma k},$$

whereas the oblique two-dimensional benchmark used in the main RLW computations has amplitude

$$A_{2D} = \frac{3(c - \alpha k - \beta \ell)}{\gamma k + \delta \ell}.$$

The oblique two-dimensional solitary wave, when β, δ, or ℓ are non-zero, will have a smaller peak than its reduced one-dimensional counterpart. Given the parameter set being discussed, this corresponds to $A_{1D} = 6$ and $A_{2D} = 4.2$. From this, we can see that the difference in peak height is consistent with the analytical frameworks of the two models and discards any formal numerical error by attributing the difference to model reduction.

The left panel of Figure 5 demonstrates that most of the final time computed solution is in agreement with the exact travelling-wave profile, which indicates that the numerical scheme conserves the amplitude and localization of the solitary structure throughout the time interval. In this respect, the estimated results are consistent with numerical analysis, as the mixed adaptive discretization is not expected to cause any abrupt phase shifts, amplitude damping, or unnecessary oscillations during long-time propagation. The right panel adds to this observation by showing the mesh trajectories in the (x, t)-plane. These trajectories show that the adaptive mechanism persistently shifts the nodes toward the active wave zone and moves them along with the localized structure as it moves through the domain. Therefore, the figure confirms two pivotal aspects of the PMA strategy: first, the dynamic mesh motion is in sync with the evolving solitary wave; and second, this synchronization is sufficient for an accurate final-time numerical approximation. Thus, the figure illustrates that the adaptive solver achieves local mesh concentration as well as accurately preserving the long-time profile for the benchmark wave (3.21).

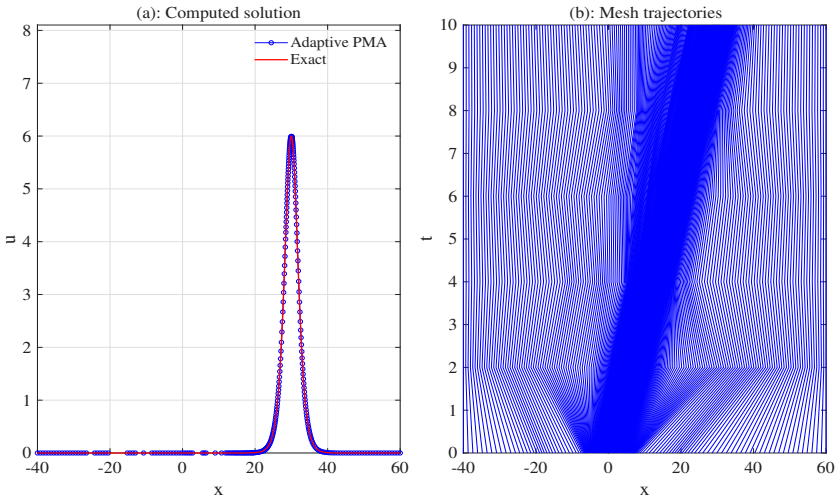

Figure 5. Final-time one-dimensional verification for the single solitary wave (3.21). Left: Computed and exact profiles at $t = 10$. Right: Mesh trajectories in the (x, t)-plane.

Unlike the single-wave benchmark, the two-pulse configuration is primarily intended to assess the robustness of the adaptive framework under more complicated multi-structure wave evolution rather than to provide a strict convergence benchmark. In this case, the simultaneous propagation and interaction of multiple localized structures lead to more complex mesh redistribution patterns and stronger sensitivity to the adaptive rezoning process. Nevertheless, the numerical results consistently

show that the PMA-based adaptive computation maintains improved local resolution and smaller visible approximation errors compared with the corresponding fixed-mesh computation throughout the simulation interval.

Figure 6 illustrates the three representative snapshots of the adaptive computation for the two-pulse reference configuration (3.22).

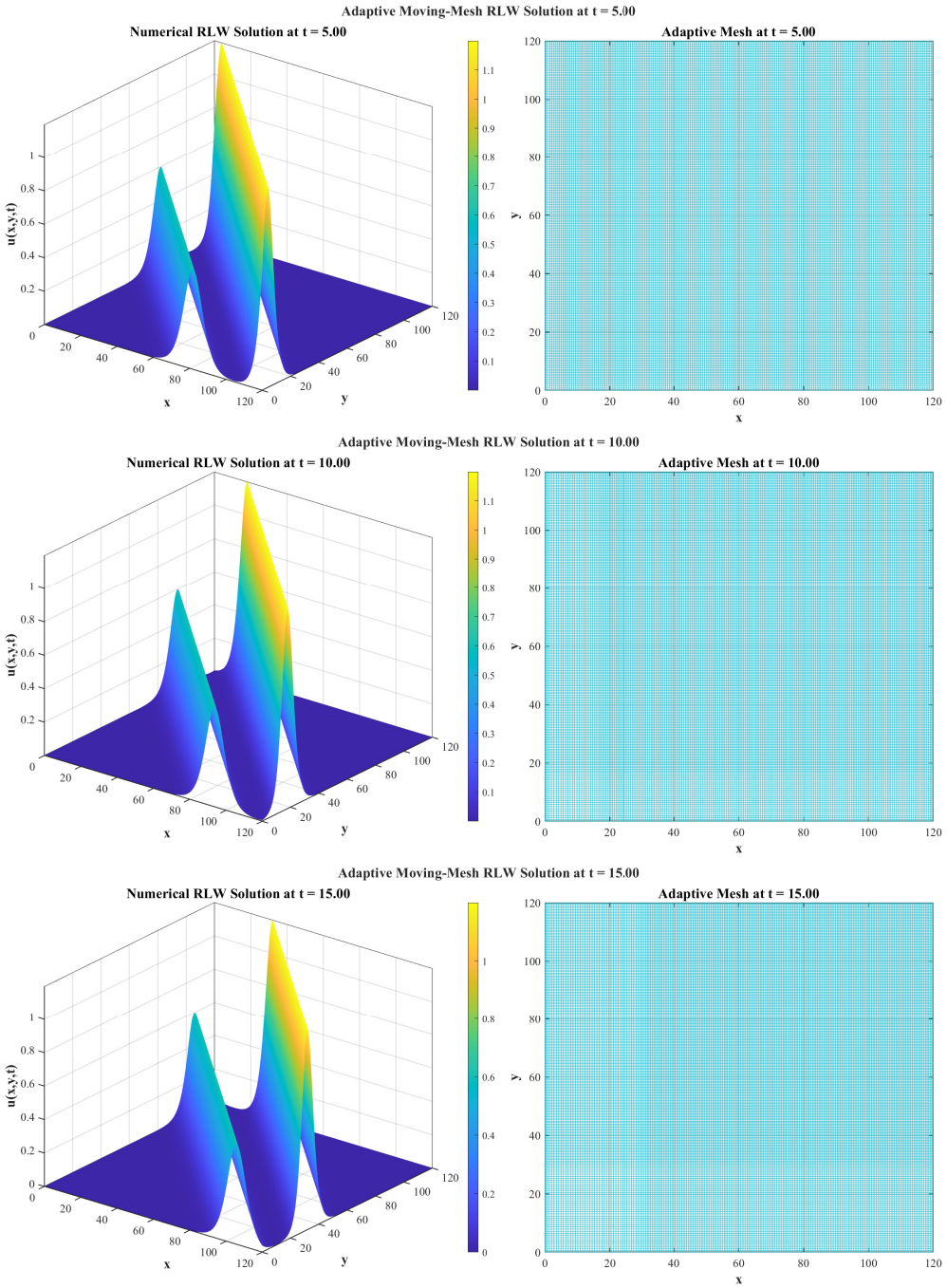

Figure 6. Adaptive evolution of the two-pulse configuration (3.22) at $t = 5$, $t = 10$, and $t = 15$. Each subfigure shows the numerical solution and the associated adaptive mesh.

The chosen times $t = 5$, $t = 10$, and $t = 15$ succinctly summarize the solution at early, intermediate, and late stages of the evolution. In all three subfigures, the numerical solution captures the two localized wave structures and shows robust coherence, indicating that the mixed adaptive discretization is robust even in the presence of multiple evolving pulses. The mesh plots demonstrate that the adaptive redistribution maintains its global regularity throughout the computation. Compared to the single-wave case, where the nodal concentration is heavily focused around a single dominant solitary core, the current two-pulse configuration results in a visually smoother and more uniform mesh response. This observation is both physically and numerically justified, as the active solution is distributed over a wider area of the computational domain and involves multiple localized structures. From the viewpoint of numerical analysis, this figure demonstrates that the PMA framework is able to adapt not only to sharply localized single-wave states, but also to more complex multi-structure configurations without introducing visible mesh distortion or loss of solution coherence.

For completeness, Table 3 summarizes the main advantages and limitations of the analytical and numerical methods used in this study.

Table 3. Summary of the main advantages and limitations of the methods used in this study.

Method	Advantages	Limitations
Riccati equation approach	Provides explicit travelling-wave solutions in a direct algebraic form. It is useful for constructing smooth benchmark profiles for numerical verification.	It is mainly constructive and symbolic. It does not by itself provide a general numerical solver for arbitrary initial data or complex wave interactions.
Generalized Arnous-type representation	Gives an alternative exact-solution construction and confirms the analytical structure of the reduced travelling-wave equation.	It may generate singular or periodic branches that are less suitable for quantitative numerical benchmarking.
Fixed-mesh computation	Simple to implement and useful as a baseline comparison. It uses the same mixed formulation, finite-difference discretization, and time integrator.	It distributes resolution uniformly, so many nodes may be wasted in inactive regions of the computational domain. localized wave cores may therefore be under-resolved.
Adaptive mixed DA–PMA framework	Concentrates mesh points near dominant wave regions. It improves local resolution and reduces the numerical errors for the same effective spatial resolution.	Its global convergence behavior is empirical because rezoning and inter-mesh interpolation introduce additional error effects. The method also requires careful monitor-parameter selection.

5. Conclusions

This study developed an adaptive mixed computational framework for the two-dimensional regularized long-wave equation. The main contribution of the work is the mixed differential–algebraic reformulation of the two-dimensional RLW equation. This formulation is combined with bidirectional PMA-based adaptive mesh redistribution on nonuniform tensor-product grids. The travelling-wave profiles constructed in the paper were employed as compatible benchmark fields for the adaptive

computations. In particular, they provided exact initial conditions, boundary values, auxiliary-field data, and reference profiles for the quantitative assessment of the proposed adaptive solver. The numerical experiments demonstrated that the adaptive framework accurately resolves localized wave structures while maintaining good mesh quality throughout the computations. The results also showed that the adaptive method produces smaller errors than the corresponding fixed-mesh discretization with comparable spatial resolution. Regarding the numerical part, the RLW equation was reformulated via an auxiliary variable, allowing for the treatment of mixed partial space-time derivatives within a differential-algebraic mixed system. The resulting differential algebraic equations were then implemented on bidirectionally adaptive non-uniform tensor-product mesh using a second-order five-point Fornberg finite difference method, along with monitor-based PMA/rezoning and shape-preserving tensor-product interpolation between successive meshes. In this case, the frozen mesh approximation was demonstrated to be second order spatially, while the adaptive approach was justified on the basis of conditional stability due to permissible mesh evolution and empirically converged due to differential approximation and rezoning.

The numerical experiment results demonstrated that the PMA-based adaptive approach is superior when compared to the uniform fixed-mesh discretization. For the solitary wave benchmark, the adaptive approach demonstrated a significant decrease in both the L^2 and L^∞ errors and high fidelity to the travelling wave profile, displaying strong empirical convergence, and maintaining it for the entire time interval.

The provided mesh diagnostics show that node redistribution remained closely aligned with the evolving localized wave core, which explains the increase in efficiency for the adaptive approximation. Further testing for the two-pulse reference configuration adds to the evidence that the same framework is robust in the wider multi-structure domain and is capable of retaining coherent solution behavior with no observable mesh deterioration.

In summary, the results presented demonstrate that the proposed adaptive mixed RLW framework achieves a good compromise in terms of mathematical rigour, geometric adaptability, and computational efficiency. The approach stands out for localized dispersive waves over large domains, especially for problem areas where uniform meshes become redundant and where mixed derivatives disrupt standard discretization. The present work naturally leads to sharper benchmark studies for interacting wave configurations, performance comparisons against other adaptive solver techniques, and applying the same mixed adaptive methodology to other nonlinear dispersive models with Sobolev-type regularization.

Author contributions

H. S. Alayachi: methodology, software, validation, visualization, writing—original draft; A. R. Alharbi: conceptualization, formal analysis, supervision, writing—review and editing. All authors have read and agreed to the published version of the manuscript.

Use of Generative-AI tools declaration

The authors used an AI-assisted language tool for language polishing and grammar checking only. All scientific content was reviewed and approved by the authors.

Acknowledgments

The authors gratefully acknowledge the support provided by Taibah University, College of Science, Department of Mathematics.

Conflict of interest

The authors declare no conflicts of interest.

References

1. D. H. Peregrine, Calculations of the development of an undular bore, *J. Fluid Mech.*, **25** (1966), 321–330. https://doi.org/10.1017/S0022112066001678
2. T. B. Benjamin, J. L. Bona, J. J. Mahony, Model equations for long waves in nonlinear dispersive systems, *Philos. Trans. A Math. Phys. Eng. Sci.*, **272** (1972), 47–78. https://doi.org/10.1098/rsta.1972.0032
3. J. A. Goldstein, B. J. Wichnoski, On the Benjamin–Bona–Mahony equation in higher dimensions, *Nonlinear Anal.*, **4** (1980), 665–675. https://doi.org/10.1016/0362-546X(80)90067-X
4. J. Avrin, J. A. Goldstein, Global existence for the Benjamin–Bona–Mahony equation in arbitrary dimensions, *Nonlinear Anal.*, **9** (1985), 861–865. https://doi.org/10.1016/0362-546X(85)90023-9
5. P. J. Olver, Euler operators and conservation laws of the BBM equation, *Math. Proc. Cambridge Philos. Soc.*, **85** (1979), 143–160. https://doi.org/10.1017/S0305004100055572
6. L. A. Medeiros, M. M. Miranda, Weak solutions for a nonlinear dispersive equation, *J. Math. Anal. Appl.*, **59** (1977), 432–441. https://doi.org/10.1016/0022-247X(77)90071-3
7. J. L. Bona, W. G. Pritchard, L. R. Scott, An evaluation of a model equation for water waves, *Philos. Trans. A Math. Phys. Eng. Sci.*, **302** (1981), 457–510. https://doi.org/10.1098/rsta.1981.0178
8. J. L. Bona, W. R. McKinney, J. M. Restrepo, Stable and unstable solitary-wave solutions of the generalized regularized long-wave equation, *J. Nonlinear Sci.*, **10** (2000), 603–638. https://doi.org/10.1007/s003320010003
9. B. Tian, W. Li, Y. T. Gao, On the two-dimensional regularized long-wave equation in fluids and plasmas, *Acta Mech.*, **160** (2003), 235–239. https://doi.org/10.1007/s00707-002-0967-0
10. W. X. Ma, B. Fuchssteiner, Explicit and exact solutions to a Kolmogorov–Petrovskii–Piskunov equation. I, *Int. J. Non-Linear Mech.*, **31** (1996), 329–338. https://doi.org/10.1016/0020-7462(95)00064-X
11. V. B. Matveev, M. A. Salle, *Darboux transformations and solitons*, Springer-Verlag, 1991. https://doi.org/10.1007/978-3-662-00922-2
12. A. R. Alharbi, Traveling-wave and numerical solutions to a Novikov–Veselov system via the modified mathematical methods, *AIMS Math.*, **8** (2023), 1230–1250. https://doi.org/10.3934/math.2023062

13. A. R. Alharbi, Traveling-wave and numerical solutions to nonlinear evolution equations via modern computational techniques, *AIMS Math.*, **9** (2024), 1323–1345. https://doi.org/10.3934/math.2024065
14. A. Ahmed, A. R. Alharbi, I. Hashim, Exact and numerical solutions of the generalized breaking soliton system: Insights into non-linear wave dynamics, *AIMS Math.*, **10** (2025), 5124–5142. https://doi.org/10.3934/math.2025235
15. A. Ahmed, A. R. Alharbi, H. S. Alayachi, I. Hashim, Exact and numerical approaches for solitary and periodic waves in a (2+1)-dimensional breaking soliton system with adaptive moving mesh, *AIMS Math.*, **10** (2025), 8252–8276. https://doi.org/10.3934/math.2025380
16. A. Ahmed, T. G. Alharbi, A. R. Alharbi, I. Hashim, Traveling wave reductions and adaptive moving mesh computations for the improved Boussinesq equation, *AIMS Math.*, **10** (2025), 28374–28395. https://doi.org/10.3934/math.20251248
17. I. Alraddadi, F. Alsharif, S. Malik, H. Ahmad, T. Radwan, K. K. Ahmed, Innovative soliton solutions for a (2+1)-dimensional generalized KdV equation using two effective approaches, *AIMS Math.*, **9** (2024), 34966–34980. https://doi.org/10.3934/math.20241664
18. F. Calogero, A. Degasperis, *Spectral transform and solitons: tools to solve and investigate nonlinear evolution equations*, North-Holland, 1982.
19. K. Spayd, M. Shearer, The Buckley–Leverett equation with dynamic capillary pressure, *SIAM J. Appl. Math.*, **71** (2011), 1088–1108. https://doi.org/10.1137/100807016
20. R. E. Showalter, Existence and representation theorems for a semilinear Sobolev equation in Banach space, *SIAM J. Math. Anal.*, **3** (1972), 527–543. https://doi.org/10.1137/0503051

AIMS Press